Linear Chains of Nanomagnets: Engineering the Effective Magnetic Anisotropy

Abhishek Talapatra and Adekunle O. Adeyeye*

Dr. Abhishek Talapatra, Prof. Adekunle O. Adeyeye
Information Storage Materials Laboratory, Department of Electrical and Computer
Engineering, National University of Singapore, Singapore 117576
E-mail: eleaao@nus.edu.sg

Prof. Adekunle O. Adeyeye
Present Address: Department of Physics, Durham University, South Rd, Durham, DH1 3LE,
UK

This paper investigates the control of effective magnetic anisotropy in Permalloy linear chain arrays, achieved by tuning the symmetry arrangements of the ellipsoidal nanomagnets and the film thickness. When the ellipsoidal nanomagnets are coupled along their easy axis, stronger effective magnetic anisotropy is achieved compared to when the nanomagnets are coupled along their hard axis. A clear transition from a single domain states to a combination of complex flux closure states such as vortex, double vortices are observed at different applied field angles when the film thickness is varied in the range from 20 nm to 100 nm. Tunable microwave absorption spectra, obtained by the ferromagnetic resonance spectroscopy established the complex interplay between the shape anisotropy and magnetostatic interactions which becomes further intriguing at different film thicknesses and applied field angles. Micromagnetic simulations are in good agreement with the experimental results. Our results demonstrate the possible ways of manipulating the effective magnetic anisotropy in the arrays of nanomagnets for magnonic and microwave applications.

1. Introduction

Nanomagnet-based memories and logic operations have attracted a lot of potential technological interest due to the nonvolatility[1] and the possibility for fabricating ultrahigh density media with thermal robustness.[2] Extensive research efforts have been reported on

1

information processing based on spin waves,[3, 4] domain-wall motion-based devices,[5, 6] coupled vortices,[7, 8] topologically stable skyrmions,[9, 10] recently ventured spin-orbit-torque driven propagating spin waves[11] for scalable devices and synchronized spin Hall nano-oscillators for neuromorphic computations.[12] It is well known that in an array of magnetic nanostructures, the magnetization reversal processes of both single-domain and multi-domain structures are significantly affected when the inter-element spacing is less than the lateral size of the element. The dipolar interaction between the elements plays a crucial role in determining the magnetic state of the system. Being a long-ranged force, dipolar interactions can be tuned by controlling the inter-element spacing between the neighboring nanomagnets (NMs) in an array, and hence the collective response is manipulated. Most of the efforts have been made to understand the role of dipolar interaction on the magnetization reversal, domain formation, nucleation, and annihilation by varying the periodicity of the NMs with different lattice arrangements.[13-15] The effect of breaking the symmetry either by the applied field angle or by the lattice arrangements on magnetization dynamics was also carried out.[16, 17] The geometry and the thickness of individual NMs play important roles in controlling the shape anisotropy and magnetostatic self-interaction due to the flux closure at the edges of the NM respectively. Magnetic nanostructures have been extensively studied in various systems for example in magnetic dots with negligible shape anisotropy,[18, 19] nanowires incorporating strong shape anisotropy,[20, 21] rectangular dots/antidots/ring/mutually-crossed nanomagnets,[22-25] reconfigurable magnonic crystal with rhomboid-shaped nanomagnets for deterministic control of magnetization dynamics,[26, 27] magnetic quantum cellular automata (MQCA) based devices[28, 29] and artificial spin ice nanostructures.[30-32]

In this paper, we demonstrate the control of effective magnetic anisotropy in linear chains of NMs by tuning the configurational anisotropy, thickness, and applied field directions. The coupled magnetic elements have been arranged in two distinct configurations, namely: type-I, where the ellipsoidal nanomagnets are arranged in such a way that the neighboring elements

are placed along the major axis of the ellipsoid, and type-II, in which the neighboring elements are coupled along the minor axis of the ellipsoid. Hence, the shape anisotropy of each NM and the configurational anisotropy due to the lattice arrangements favor the same direction of magnetization for type-I arrays while competition exists between the shape and configurational anisotropy for type-II arrays. Owing to have negligible magneto-crystalline anisotropy, Permalloy (Py, $Ni_{80}Fe_{20}$) was used to conduct a systematic comparison for the static and dynamic behavior between the two types of configurations to understand the role of configurational anisotropy and dipolar coupling by varying the coupling schemes and film thickness (d). Our results depict the transition from a single domain or oppositely magnetized domains state to the combination of complex flux closure characteristics, containing elongated single vortex or double vortices configurations with increasing thickness and at the different applied magnetic field (H_{app}). The results of the magnetization dynamics study clearly show a systematic trend of variation of the spin wave modes with thicknesses and applied field angles (ϕ) for the two types of arrays. The experimental results are strongly complemented with micromagnetic simulations using OOMMF software[33] to present the space-frequency resolved localization of the spin wave modes. Our work shows potential significance for the recently highlighted techniques for microstate-controlled dynamics,[34] NM-specific magnetic writing, and tunable spectrum-selection devices for microwave filter applications with reprogrammable magnonic crystal.[35, 36]

2. Results and Discussions

The scanning electron microscope (SEM) images of type-I and type-II arrays of linear chains (LC) are shown in **Figure 1**a and d respectively. The SEM images confirm a good lift-off and uniformity of the nanostructures over a large area. The length of the major axis (l) and minor axis (w) for individual ellipsoidal NM is around 480 nm and 235 nm respectively for both types of arrays. It is evident that the edge to edge distance between two neighboring NMs

along l (D_l) is 105 nm for type-I LC which is much smaller compared to the value of l and the distance between the neighboring NMs along w (D_w) is 350 nm, more than the value of w. The lattice arrangement is reversed for type-II LC, where D_w is measured to be around 52 nm and the value of D_l is around 1020 nm. Thus, it can be confirmed that magnetostatic interactions play a dominant role along l for type-I and along w for type-II LC.

2.1. Static Magnetic Properties

The thickness-dependent hysteresis loops for type-I arrays are shown in **Figure 1**b and c for $\phi = 0°$ and 90°respectively. A schematic of the direction of H_{app} relative to the lattice arrangement is shown in the inset of **Figure 1**a. It is clear that $\phi = 0°$ indicates the field direction along the major axis of the NMs. As expected, the saturation magnetization (M_s) increases with d due to the increase in the volume of the magnetic materials. The static magnetic properties, such as remanence to saturation magnetization ratio (M_R/M_s), coercive field (H_c), and saturation field (H_s) change significantly with the variation in d and ϕ and are recorded in **Table 1** for both type-I and type-II arrays of NMs. From **Figure 1**b, almost perfectly rectangular-shaped hysteresis loop with high M_R/M_s with an abrupt magnetization reversal close to H_c can be observed for $d = 20$ nm at $\phi = 0°$. This hysteresis loop suggests a higher energy state of the NMs which makes a favorable condition for stable single domain magnetic nano-islands at remanence. The features of the reversal become significantly different for $d = 50$ nm. A multiple-step switching of magnetization can be observed from **Figure 1**b where the first switching occurs at a field of 30 Oe. The slope of the hysteresis curve decreases thereafter with a plateau-like region from 90 to 220 Oe at which the second switching occurs and leads to the reverse saturated state. This multiple switching suggests that all the NMs do not have a similar state of magnetization which broadens the switching field distribution. The reduction in M_R/M_s and H_c with the increase in thickness from 20 to 50 nm of the type-I arrays (**Table 1**) suggests that few of the NMs deviate from the single domain state at remanence which initiates the

4

reversal at lower H_{app}. For the 100 nm thick type-I arrays (**Figure 1**b), the magnetostatic energy drives the onset of the reduction in magnetization at a higher nucleation field of around 380 Oe. Further reduction in the field value leads to a reversible and linear dependence of magnetization over the field range of ±280 Oe. For Py nanostructures with zero magnetocrystalline anisotropy, the linear decrease of magnetization with almost zero M_R/M_s and H_c (**Table 1**) essentially suggests favorable nucleation, growth, and annihilation of vortices could be the probable mechanism behind the magnetization reversal. The hysteresis loops for the type-I LC are significantly different for $\phi = 90°$ as shown in **Figure 1**c. For $d = 20$ nm, the magnetization drops almost linearly from 400 Oe and reaches the reverse saturation (**Figure 1**c) with much reduced M_R/M_s and H_c when compared to those values along $\phi = 0°$ (**Table 1**). In contrast, the nucleation field increases to around 1 kOe and 2 kOe for $d = 50$ nm and 100 nm respectively with negligible M_R/M_s and H_c, as shown in **Figure 1**c. The appearance of a tiny hysteresis effect near the remanence may exist due to slight sample imperfection.[37, 38] The hysteresis loops for $d = 30$ nm and 70 nm are shown in **Figure S1** of the supporting information. This can be observed from **Table 1** that the values of H_c and M_R/M_s for 30 and 70 nm thick nanostructures are comparable to those values for 20 and 100 nm thick type-I LC respectively which infers the similarity in reversal mechanism. As expected, **Table 1** depicts that the value of H_s is much higher along $\phi = 0°$ compared to that along $\phi = 90°$ indicating that the direction of the easy axis for type-I LC is along $\phi = 0°$ as the demagnetization field gets minimized along the major axis of the ellipsoidal NMs.

The thickness-dependent magnetization reversal behavior for the type-II arrays is shown in **Figure 1**e and f with H_{app} along 0° and 90° respectively. As shown in **Figure 1**e, the abrupt decrease in magnetization indicates that the formation of single-domain magnetic islands may not be energetically favorable for 20 nm thick type-II LC, instead, the formation of the domain wall is expected. Slanted hysteresis loops can be observed for both 50 and 100 nm thick arrays where the values of the nucleation fields are around 360 Oe and 900 Oe respectively (**Figure**

1e). The formation of complex spin textures including vortex and other flux-closure states is highly probable for these cases. The hysteresis behavior for 20 nm thick type-II NMs at $\phi = 90°$ (**Figure 1**f) shows comparable M_R/M_s values to that along $\phi = 0°$ (**Table 1**). The hysteresis loops for 50 and 100 nm thick type-II arrays in **Figure 1**f depict a common feature of slanted loops where the values of the nucleation fields are around 600 Oe and 1.17 kOe respectively. **Table 1** confirms that the values of H_s are still lower along $\phi = 0°$ for type-II LC and hence can be designated as the easy axis which agrees with the earlier report.[15]

The comparison between the two lattice arrangements of type-I and type-II arrays clearly shows that the value of H_s is lower for type-I arrays along the easy axis ($\phi = 0°$) and much higher along the hard axis ($\phi = 90°$) compared to type-II arrays at a constant d (**Table 1**). It is worth mentioning that the difference between the values of H_s along 0° and 90° (ΔH_s) is much lower in type-II arrays compared to that of type-I. For type-II arrays, ΔH_s is a maximum of 250 Oe at $d = 20$ nm and decreases to 150 and 125 Oe with the increase in thickness to 50 and 100 nm respectively. An opposite behavior is noted for type-I arrays, where the value of ΔH_s is around 500 and 800 Oe for 20 and 50 nm thick arrays respectively and reaches maximum to 1.25 kOe for $d = 100$ nm. The variation of ΔH_s proves that the effective anisotropy is higher for type-I arrays and shows an increasing trend with the increase in thickness which becomes exactly reversed for the type-II arrays due to the interplay between the magnetostatic self-interaction (due to the thickness) and interactions with the neighboring NMs. Hence, our results establish a viable way for the distinct control of the effective anisotropy in the arrays of NMs with the variation in lattice arrangements and the thickness of the magnetic islands.

To confirm the mechanism for thickness-dependent magnetization reversal, magnetic force microscopy (MFM) was performed at the remanent state of the two types of arrays with the direction of H_{app} along 0°, 45°, and 90°. The MFM images at $\phi = 0°$ and 90° are depicted in **Figure 2** whereas the same for $\phi = 45°$ are shown in **Figure S2** of the supporting information. Single domain magnetic states are evident from **Figure 2**a for 20 nm thick type-I arrays, the

formation of which is well supported by the rectangular hysteresis loop of **Figure 1**b. The magnetic microstructure along the hard axis for 20 nm thick type-I arrays (**Figure 2**b) also depicts a single domain features with a possible curl of magnetization at the edges due to the competition between the magnetostatic inter-island and self-interactions. Complex spin states, comprising of distorted single domain states (similar to C or S states) and single vortex states (shown by a dotted ellipse) of different chirality can be observed for 50 nm thick type-I LC at $\phi = 0°$, as shown in **Figure 2**a. The density of vortex states increases when H_{app} is applied along the hard axis (**Figure 2**b). The nucleation of the vortex and other flux closure states is responsible for minimizing the total energy of the system with reduced M_R/M_s, as observed in **Figure 1**c. Single domain states are no longer observed with the increase in thickness up to 100 nm. From **Figure 2**a, all the NMs display single elongated vortex-like states (shown by the dotted circle) with higher magnetic contrast for $d = 100$ nm. The polarity of the vortex core could not be confirmed due to the resolution limit of MFM. On the other hand, the presence of single vortex states at different core position and multiple vortex states (shown by the dotted rectangle) such as double vortex states with the vortex cores originating at the opposite corners of the NM can be observed for 100 nm thick type-I arrays at $\phi = 90°$, as shown in **Figure 2**b. The transition from single domain state to vortex state with increasing thickness agrees well with our earlier report on the artificial spin ice system[30] and the evolution of complex spin states was reported previously as a function of the spacing between the neighboring NMs in similar LC arrays.[13-15]

The MFM images for type-II arrays are depicted in **Figure 2**c and d for $\phi = 0°$ and 90° respectively. From **Figure 2**c we observe the presence of a domain wall that breaks the single domain configuration and responsible for the reduction of M_R/M_s for 20 nm thick type-II LC compared to that of type-I at $\phi = 0°$. The nucleation of a single vortex with lower magnetic contrast is observed when H_{app} is applied along 90°, as shown in **Figure 2**d. The vortex formation becomes clearer in 50 nm thick type-II LC along both the direction of H_{app} where the

combination of single vortex states and flux closure states is observed from **Figure 2**c. All the NMs show a single vortex state with the same chirality, manifesting a perfect ferromagnetic order, as depicted in **Figure 2**d for $d = 50$ nm. Extended single vortex-like states populated the majority of the NMs for the 100 nm thick type-II arrays, as observed in **Figure 2**c and d. The MFM images successfully explain the variation of spin configurations at remanence with the variation in d and ϕ for both the lattice arrangements of the NMs which are in good agreement with the static magnetic properties of the systems, measured by the superconducting quantum interference device (SQUID).

3-D Micromagnetic simulation was carried out to complement the experimental results. The dimension of the individual NM and the gap between the consecutive NMs with the featured geometry of type-I and type-II LC were extracted from the SEM images of **Figure 1**a and d respectively. However, the simulation time was minimized by scaling the entire geometry to a single row and a single column of five NMs to mimic the type-I and type-II arrays respectively. 2-D periodic boundary condition was applied to avoid the effect of truncation. The input parameters for Py include exchange constant $A = 1.05 \times 10^{-6}$ erg.cm^{-1}, $M_s = 820$ emu.cm^{-3}, zero magnetocrystalline anisotropy (K_u) and the gyromagnetic ratio $\gamma = 2.8$ GHz.kOe^{-1}. The volume of individual cells was chosen to be $(5 \text{ nm})^3$ with a random direction of initial magnetization to solve the Landau-Lifshitz-Gilbert (LLG) equation.[39] The thickness-dependent simulated hysteresis loops for type-I LC are shown in **Figure 3**a and b for $\phi = 0°$ and $90°$ respectively. We observed an almost rectangular hysteresis loop with large H_c and M_R/M_s for $d = 20$ nm and a step-like switching at 220 Oe and 100 Oe followed by a linear change in magnetization within the field range of ± 100 Oe for the 50 nm thick type-I LC along $\phi = 0°$, as shown in **Figure 3**a. The 100 nm thick type-I LC shows loop openings near both the saturation fields followed by a linear decay of magnetization, yielding negligible H_c and M_R/M_s (**Figure 3**a). Along $\phi = 90°$ (**Figure 3**b), the values of M_R/M_s and H_c decrease and H_s increases for 20 nm thick film compared to that along $\phi = 0°$. The slanted hysteresis loops are evidenced in **Figure 3**b for 50

8

and 100 nm thick type-I arrays where the value of H_s increases with the increasing film thickness, similar to the experimental findings. As expected, **Figure 3**c shows the presence of single-domain magnetic nano-islands for 20 nm thick type-I LC at $\phi = 0°$ and two oppositely magnetized domains, separated by a domain wall can be observed at $\phi = 90°$. The presence of elongated vortex with the same chirality for all the NMs in the array is evidenced for $d = 50$ nm at $\phi = 0°$. However, NMs with two different chiralities of the vortices are observed at $\phi = 90°$ (**Figure 3**c). Interestingly, double vortex diamond-like structure having the coexistence of two vortices of opposite chiralities is observed for the 100 nm thick type-I arrays along $\phi = 0°$ whereas elongated single vortex gets stabilized in which the core is shifted towards the left edge of the corresponding NM along $\phi = 90°$ (**Figure 3**c). The simulated hysteresis loops for type-II LC are shown in **Figure 3**d and e for $\phi = 0°$ and $90°$ respectively. As shown in **Figure 3**d, a broader hysteresis loop with a large M_R/M_s is observed for 20 nm thick type-II arrays whereas slanted loops are observed for $d \geq 50$ nm. The trend of the hysteresis phenomenon remains similar in **Figure 3**e at $\phi = 90°$ where the values of M_R/M_s and H_c reduce significantly with respect to those at $\phi = 0°$ for $d = 20$ nm. The value of H_s increases with d for all the samples, shown in **Figure 3**d and e. Following **Table S1** of the supporting information, it is worth mentioning that, H_s for type-II arrays is larger than that for type-I arrays along $\phi = 0°$ and the trend is opposite along $\phi = 90°$, irrespective of the film thickness. The value of ΔH_s for type-I LC increases with d, indicating maximum effective anisotropy for the 100 nm thick NMs. On the contrary, ΔH_s is negligible for the thicker (70 and 100 nm) type-II LC when compared to that of type-I LC. This can be correlated to the thickness-dependent modification of the effective anisotropy for different lattice arrangements of the NMs in which negligible difference in the demagnetization energy (not shown) was observed along the two directions of ϕ for thicker type-II LC. The simulated spin configurations at remanence for the type-II arrays at different d and ϕ are shown in **Figure 3**f. Broadly, for $d = 20$ nm, single domain nano-islands and oppositely magnetized domains are observed along $\phi = 0°$ and $90°$ respectively. Single

vortex state with same chirality of the core (situated at the middle of the NM) for all the NMs can be observed for 50 nm thick type-II arrays and elongated single vortex state with the cores of different chiralities, shifted towards either of the edges of the NMs is seen for $d = 100$ nm along both the directions of ϕ (**Figure 3**f). Micromagnetic simulations qualitatively agree with the experimental results in explaining the thickness-dependent variations of the hysteresis behavior along with the transformation from single-domain magnetic states to the complex spin configurations at remanence containing vortex, double vortices structures.

2.2. Magnetization Dynamics

To investigate the effect of thickness, geometry, and applied field angle on the magnetization dynamics, ferromagnetic resonance (FMR) studies were carried out. The representative FMR spectra (derivative of the power absorption (dP/dH) as a function of H_{app}) for type-I LC at a fixed excitation frequency (f) of 12 GHz for different d and ϕ are shown in **Figure 4**a. We observe two peaks H_{1a} and H_{1b} at 1.94 and 1.41 kOe respectively for 20 nm thick type-I arrays where H_{1a} represents the first fundamental mode with maximum intensity. Both modes show a regular field dispersion with the change in f. The intensity of the second mode H_{1b} is much lower compared to that of H_{1a}. The first fundamental mode appears due to the power absorption at the center of each NM and hence it is the central mode of maximum intensity. The other mode originates as the nodal lines or the edge modes due to strong shape anisotropy of the individual NM.[3] The first fundamental modes for the 50 and 100 nm thick films are indicated as H_{2a} (2.61 kOe) and H_{3a} (3.72 kOe) respectively where the values of the resonance field (H_R) are higher compared to that for 20 nm thick nanostructure. The FMR response at the different direction of H_{app} can be explained by the Kittel's formula,[40]

$f = \frac{\gamma}{2\pi} \sqrt{[\{H_{app} + (N_z - N_H).4\pi M_s\} \times \{H_{app} + (N_{H\perp} - N_H).4\pi M_s\}]}$, where N_H and $N_{H\perp}$

denote the demagnetizing factors along H_{app} and perpendicular to H_{app} respectively, N_z is the demagnetizing factor acting along the thickness of the film. As the magnetic field was varied

at a constant f, we will discuss our results in terms of H_R to describe the same physics as in the case of frequency sweep at a constant H_{app}. From the magnetization measurements of **Figure 1**, it is evident that the net magnetic moment of the sample increases with d. The demagnetizing factor N_z also increases with the increase in thickness. Hence, $\phi = 0°$ being the easy axis for type-I NMs, the trend of increase in H_R with d (**Figure 4**a) can be supported in the light of Kittel's formula. In continuation of the FMR spectra for type-I NMs, shown in **Figure 4**a, this can be observed that at $\phi = 45°$, the values of H_R for the first fundamental modes for 20 nm (H_{1c}) and 50 nm (H_{2b}) thick arrays are close to 1.64 kOe whereas that for 100 nm thick array decreases to 1.31 kOe (H_{3b}). A marked difference in the H_R can be observed for $\phi = 90°$ which is the hard axis of type-I arrays. The first fundamental modes appear at 1.31 kOe (H_{1d}), 1.09 kOe (H_{2d}) and 0.92 kOe (H_{3e}) for the $d = 20$, 50 and 100 nm respectively. Firstly, the values of H_R for $\phi = 90°$ is much lower than that for $\phi = 0°$ which occurs due to the increased demagnetizing field (H_d) along the direction of H_{app} for N_H being larger than $N_{H\perp}$ along $\phi = 90°$. Importantly, the trend in the variation of H_R with d is opposite for $\phi = 90°$ compared to that along $\phi = 0°$, as seen in **Figure 4**a. Now, H_d can be expressed as, $H_d = \frac{d}{D_w} \cdot M_s,$[41] where D_w and M_s remain constant. Thus, increase in thickness enhances H_d. Thus, the value of the effective magnetic field ($H_{eff} = H_{app} - H_d$) is lowest for $d = 100$ nm along $\phi = 90°$ and results in the lowest H_R along the hard axis where strong H_d dominates over the magnetization of the NMs. The variation of f and H_R of the first fundamental modes at different d for three different values of ϕ is shown in **Figure 5**a. This supports the above discussions where we observe a reverse behavior of H_R with d at $\phi = 0°$ and $90°$ with a significant crossover of H_R at different d along $\phi = 45°$ for the type-I arrays. Kittel's formula suggests an increase in resonance frequency with the increase in applied field values which can be directly observed from **Figure 5**a for all the first fundamental modes obtained from type-I arrays of different thicknesses. The intensities of the other modes, denoted by H_{2c} for $d = 50$ nm, H_{3c}, H_{3d} for $d = 100$ nm along ϕ

$= 45°$ along with H_{1e} for $d = 20$ nm, H_{2e} for $d = 50$ nm, H_{3f} for $d = 100$ nm along $\phi = 90°$ are

extremely diminished compared to the corresponding first fundamental modes. However, these

modes do not exhibit such clear thickness dependence as observed for the first fundamental

modes but show a regular field dispersion with the change in frequency, obeying the Kittel's

formula.

The representative FMR spectra for type-II NMs are shown in **Figure 4**b for different ϕ.

For $\phi = 0°$, type-II NMs also show an increasing trend of H_R with d where H'_{1a} (1.7 kOe), H'_{2a}

(2.06 kOe), and H'_{3a} (2.42 kOe) denote the positions of the first fundamental modes for 20, 50

and 100 nm thick LC respectively. However, at a constant f and $\phi = 0°$, the comparison between

Figure 4a and b infers that the value of H_R is larger for type-I NMs and the difference in H_R

between the type-I and type-II NMs increases with increasing thickness. This can be attributed

to the fact that the lattice arrangement of the NMs where the shape anisotropy of the individual

NM and the configurational anisotropy due to the spatial arrangement favor the same direction

of the magnetization in type-I arrays. For type-II, however, there is a competition between the

shape and configurational anisotropy resulting in a reduction in the effective anisotropy, which

has also been confirmed from the static magnetic properties, presented earlier. Thus, type-II

NMs experience larger demagnetization than type-I for the same d and hence smaller H_R.

Similar to the case of type-I, the intensity of the other modes such as H'_{1b}, H'_{2b} and H'_{3b} with

H'_{3c} for 20, 50 and 100 nm thick LC respectively are less compared to that of the corresponding

fundamental modes, expected to appear at the central region of the NMs. For $\phi = 45°$ (**Figure**

4b), the fundamental modes for type-II arrays appear at H'_{1c} (1.65 kOe) and H'_{2c} (1.83 kOe) for

$d = 20$ and 50 nm respectively, and are close to H_{1c} and H_{2b}, the corresponding fundamental

modes for type-I arrays, shown in **Figure 4**a. However, the frequency of the mode at H'_{3d} (2.16

kOe) for 100 nm thick type-II arrays is higher in magnitude compared to H_{3b} of type-I arrays.

Interestingly, the variation of H_R with d for type-II arrays (**Figure 5**b) is significantly different

when compared to that of type-I arrays for $\phi = 90°$. According to **Figure 4**b, H'_{1e} (1.57 kOe), H'_{2e} (1.66 kOe) and H'_{3f} (2 kOe) are the fundamental modes for 20, 50 and 100 nm thick LC respectively for $\phi = 90°$. In this case, the values of H_R are larger in type-II arrays and show an increasing trend with respect to d. From the hysteresis loops of **Figure 1**, we inferred that type-I arrays display larger effective anisotropy which increases with the increase in thickness. The thickness dependence of ΔH_s for type-II arrays is also opposite to that of type-I arrays. Thus, the increasing trend of H_R has been observed with d (**Figure 5**b) along the hard axis ($\phi = 90°$) for the type-II arrays, which is reversed for the type-I arrays. The contrast in thickness-dependent magnetization dynamics become distinct from **Figure 5**b when compared with **Figure 5**a. All the fundamental modes in type-II arrays follow the Kittel's formula (**Figure 5**b) and do not show ϕ dependent cross-over of H_R at different d, unlike the case in **Figure 5**a for $\phi = 45°$. The presence of low-intensity modes such as H'_{1d}, H'_{2d}, H'_{3e} at $\phi = 45°$ and H'_{1f}, H'_{2f}, H'_{3g} at $\phi = 90°$ for 20, 50, 100 nm thick films respectively can be evidenced for type-II arrays. The dispersion of the other low-intensity modes also follows the Kittel's formula (not shown). It is worth mentioning that, we have observed additional modes at lower field values, especially for the thicker films. The frequency dispersion of those modes is not regular with the applied field and hence not discussed in this paper. Those modes may originate due to the inhomogeneity of magnetization (vortex states) at lower field values or stronger demagnetization near the edges or presence of the structural inhomogeneities created during the sample fabrication processes.

To simulate the dynamic response and to investigate the localization of the power absorption profile at the resonance frequencies, the saturated state of magnetization was obtained by applying 2.5 kOe of H_{app}. For the dynamic simulations, the value of the damping factor (α) was set at 0.008, close to the value of bulk Py. A sinc pulse of amplitude 50 Oe was used perpendicular to the plane of the sample to perturb the magnetization, variation of which

was recorded up to 5 ns within which it completely damps out. The sampling interval was fixed at 10 ps. Fast Fourier transform (FFT) was used to transform the time-resolved magnetization data in the frequency domain. Thus, we obtain the simulated FMR response of the LC arrays as a function of frequency at a constant H_{app} along with the space-frequency resolved 2-D mode profiles of the power absorption at the corresponding resonance frequencies. Further detail about the dynamic simulation can be found elsewhere.[42]

The simulated dynamic response at H_{app} = 2.5 kOe is shown in **Figure 6**a and c for the 50 nm thick type-I and type-II arrays respectively as a function of ϕ. From the hysteresis loops of **Figure 3**, it is clear that H_{app} = 2.5 kOe is large enough to saturate the samples. For type-I arrays, **Figure 6**a shows the presence of two distinct peaks for each value of ϕ and the intensity of the first fundamental mode is much higher compared to the other mode, similar to the experimental data of **Figure 4**. The modes corresponding to f_{1a} (17.2 GHz), f_{2a} (14.4 GHz) and f_{3a} (11.6 GHz) in **Figure 6**a are designated as the first fundamental modes along ϕ = 0°, 45°, and 90° respectively. The 2-D mode profiles for power absorption corresponding to the mentioned frequencies are shown in **Figure 6**b. It is evident that the modes at f_{1a} and f_{3a} are located at the central region of the NMs where the absorption profile is perpendicular to the direction of the applied field. The second modes in **Figure 6**a are located at f_{1b} (14 GHz) and f_{3b} (8.6 GHz) for ϕ = 0° and 90° respectively, mode profiles (**Figure 6**b) of which display the nodal lines at the center along with feeble absorption near the edges of the NMs. The mode profiles for f_{2a} (14.4 GHz) and f_{2b} (15.2 GHz) at ϕ = 45° show non-uniform power absorption throughout the entire NMs along with the absorption near the edges (**Figure 6**b). This may be attributed to the presence of an equal and opposite distribution of the magnetic field along both the longitudinal and transverse direction of the NMs. The mode profiles in **Figure 6**b show inhomogeneity in the absorption where stronger absorption can be observed for the NMs located in the central area. This demonstrates the presence of stronger demagnetization near the two edges of the simulation area only for the type-I arrays. The simulated FMR spectra for type-II arrays (**Figure**

6c) also show the presence of two peaks for each orientation of H_{app}. The first fundamental

modes are located at f'_{1a} (15 GHz), f'_{2a} (14.2 GHz) and f'_{3a} (14.4 GHz) for $\phi = 0°$, 45°, and 90°

respectively. The corresponding 2-D mode profiles of **Figure 6**d depict the absorption near the

central part of the NMs and appear to be uniform for all the NMs in the array for f'_{1a} and f'_{3a}.

Similar to the response in the type-I array, the second modes f'_{1b} (12.8 GHz) and f'_{3b} (10.8 GHz)

for $\phi = 0°$ and 90° respectively display the nodal lines near the center of the NMs (**Figure 6**d).

The mode profiles at $\phi = 45°$ for f'_{2a} (14.2 GHz) and f'_{2b} (10.8 GHz) depict non-uniform

absorption throughout the entire NMs (**Figure 6**d). Thus, micromagnetic simulations reveal the

presence of two prominent modes that appear near the central part of the NMs in the form of

localized continuous absorption and discrete nodal lines for both types-I and type-II arrays

along the longitudinal and transverse direction of the applied field. The simulated FMR spectra

also showed the presence of less-intense, low-frequency edge modes which are not shown here.

The features of the mode profiles corresponding to the thicker and thinner films are similar to

that of the representative 50 nm thick film and hence not shown separately. Importantly, the

difference between the frequencies of the fundamental modes along $\phi = 0°$ and 90° is larger for

type-I array (5.6 GHz) compared to that in type-II (0.6 GHz), similar to the experimental

observations (**Figure 4**), explained in terms of H_R. Thus, we have shown tunability of the static

and dynamic magnetic properties of Py NMs with lattice arrangements, film thickness, and

applied field angles. The experimental results and micromagnetic simulations are in good

agreement.

3. Conclusion

In summary, we have demonstrated how to control the effective magnetic anisotropy in

linear chains of Permalloy NMs. Stronger effective magnetic anisotropy is achieved when the

ellipsoid NMs are coupled along their major axis as compared to the lattice arrangement when

they are coupled along the minor axis. Systematic static and dynamic magnetic measurements

established an opposite trend of variation of the effective anisotropy with film thickness for type-I and type-II LC. A thickness-dependent transition from single domain states to complex spin states containing single vortex, multiple vortices are observed. The variation of FMR spectra at various thicknesses and applied field angles established different interplay between the shape anisotropy and the magnetostatic interactions for both the arrays. There is a good agreement between the experimental results and micromagnetic simulations. The results show potential applicability in magnetic logic circuits, island-specific control of magnetic properties, and microwave filter devices.

4. Experimental Section

Fabrication: The type-I and type-II linear chains of NMs were patterned over a large area of 4 mm × 4 mm in a 240 nm thick resist film on top of a 60 nm thick bottom antireflection coating on silicon substrates using deep ultraviolet (DUV) lithography at an exposure wavelength of 193 nm. Details of the fabrication process have been described elsewhere.[43] To obtain the linear chain structures from the resist pattern, a 5 nm thick Cr adhesive layer followed by Py layer of various thicknesses, in the range from 20 nm to 100 nm were deposited on the two lattice configurations using electron beam evaporation at room temperature at a deposition rate of 0.2 Å/sec with a base pressure of 5×10^{-8} Torr. The deposition process was followed by an ultrasonic lift-off process in OK73 resist thinner.

Characterizations: The completion of the lift-off process was confirmed by SEM imaging. The collective magnetization reversal mechanism was probed using a SQUID magnetometer. The magnetic ground states were directly imaged by MFM at a fixed tip lift height of 75 nm for all the samples. Before the MFM imaging, the samples were saturated in an applied field of 8 kOe and then brought back to zero to establish the remanent state. The dynamic properties were characterized using broadband FMR spectroscopy with a sweeping field in the range of ±4.5 kOe. A vector network analyzer (VNA) was used to excite the samples globally with an

excitation frequency, which was varied in the range of 10-16 GHz. The derivative of the power

absorption at resonance was detected by a lock-in amplifier.

Supporting Information
Supporting Information is available from the Wiley Online Library or from the author.

Conflict of Interest
The authors declare no conflict of interest.

Received: ((will be filled in by the editorial staff))
Revised: ((will be filled in by the editorial staff))
Published online: ((will be filled in by the editorial staff))

References

[1] B. Dieny, R. B. Goldfarb, K-J. Lee, *Introduction to Magnetic Random-Access Memory*, John Wiley & Sons, Inc., Hoboken, NJ, USA **2017**.

[2] O. Hellwig, E. E. Marinero, D. Kercher, T. Hennen, A. McCullum, E. Dobisz, T-W. Wu, J. Lille, T. Hirano, R. Ruiz, M. K. Grobis, D. Weller, T. R. Albrecht, *J. Appl. Phys.* **2014**, *116*, 123913.

[3] A. Haldar, A. O. Adeyeye, *ACS Nano* **2016,** *10* (1), 1690-8.

[4] B. Rana, Y. Otani, *Phys. Rev. Appl.* **2018,** *9* (1).

[5] Z. Luo, A. Hrabec, T. P. Dao, G. Sala, S. Finizio, J. Feng, S. Mayr, J. Raabe, P. Gambardella, L. J. Heyderman, *Nature* **2020,** *579* (7798), 214-218.

[6] K. A. Omari, T. J. Broomhall, R. W. S. Dawidek, D. A. Allwood, R. C. Bradley, J. M. Wood, P. W. Fry, M. C. Rosamond, E. H. Linfield, M.-Y. Im, P. J. Fischer, T. J. Hayward, *Adv. Funct. Mater.* **2019,** *29* (10).

[7] A. Hierro-Rodriguez, C. Quirós, A. Sorrentino, R. Valcárcel, I. Estébanez, L. M. Alvarez-Prado, J. I. Martín, J. M. Alameda, E. Pereiro, M. Vélez, S. Ferrer, *Appl. Phys. Lett.* **2017,** *110* (26).

[8] S. Mondal, S. Barman, A. Barman, *J. Magn. Magn. Mater.* **2020,** *502*.

[9] S. Luo, M. Song, X. Li, Y. Zhang, J. Hong, X. Yang, X. Zou, N. Xu, L. You, *Nano Lett.* **2018,** *18* (2), 1180-1184.

[10] G. Yu, P. Upadhyaya, Q. Shao, H. Wu, G. Yin, X. Li, C. He, W. Jiang, X. Han, P. K. Amiri, K. L. Wang, *Nano Lett.* **2017,** *17* (1), 261-268.

[11] H. Fulara, M. Zahedinejad, R. Khymyn, A. A. Awad, S. Muralidhar, M. Dvornik, J. Akerman, *Sci. Adv.* **2019**, *5*, eaax8467.

[12] M. Zahedinejad, A. A. Awad, S. Muralidhar, R. Khymyn, H. Fulara, H. Mazraati, M. Dvornik, J. Akerman, *Nat. Nanotechnol.* **2020,** *15* (1), 47-52.

[13] D. Bisero, P. Cremon, M. Madami, M. Sepioni, S. Tacchi, G. Gubbiotti, G. Carlotti, A. O. Adeyeye, N. Singh, S. Goolaup, *J. Nanopart. Res.* **2011,** *13* (11), 5691-5698.

[14] X. Yin, S. H. Liou, A. O. Adeyeye, S. Jain, B. Han, *J. Appl. Phys.* **2011,** *109* (7).

[15] S. Jain, A. O. Adeyeye, N. Singh, *Nanotechnology* **2010,** *21* (28), 285702.

[16] J. Ding, S. Jain, A. O. Adeyeye, *J. Appl. Phys.* **2011,** *109* (7).

[17] W. Bang, F. Montoncello, M. T. Kaffash, A. Hoffmann, J. B. Ketterson, M. B. Jungfleisch, *J. Appl. Phys.* **2019,** *126* (20).

[18] M. Madami, G. Gubbiotti, S. Tacchi, G. Carlotti, *J. Phys. D: Appl. Phys.* **2017,** *50* (45).

[19] X. Zhou, D. Kumar, I. S. Maksymov, M. Kostylev, A. O. Adeyeye, *Phys. Rev. B* **2015,** *92* (5).

[20] L. L. Xiong, A. O. Adeyeye, *Appl. Phys. Lett.* **2016,** *108* (26).

[21] L. L. Xiong, M. Kostylev, A. O. Adeyeye, *Phys. Rev. B* **2017,** *95* (22).

[22]   B. Rana, D. Kumar, S. Barman, S. Pal, R. Mandal, Y. Fukuma, Y. Otani, S. Sugimoto, A. Barman, *J. Appl. Phys.* **2012,** *111* (7).

[23]   X. Zhou, E. V. Tartakovskaya, G. N. Kakazei, A. O. Adeyeye, *Phys. Rev. B* **2017,** *96* (2).

[24]   S. Choudhury, S. Majumder, S. Barman, Y. Otani, A. Barman, *Phys. Rev. Appl.* **2018,** *10* (6).

[25]   K. Adhikari, S. Barman, R. Mandal, Y. Otani, A. Barman, *Phys. Rev. Appl.* **2018,** *10* (4).

[26]   A. Haldar, A. O. Adeyeye, *Appl. Phys. Lett.* **2016,** *108* (16).

[27]   A. Haldar, D. Kumar, A. O. Adeyeye, *Nat. Nanotechnol.* **2016,** *11* (5), 437-43.

[28]   A. Imre, G. Csaba, A. Orlov, G. H. Bernstein, W. Porod, *Science* **2006**, *311* (5758), 205-208.

[29]   A. Orlov, A. Imre, G. Csaba, L. Ji, W. Porod, G. H. Bernstein, *J. Nanoelect. Optoelect.* **2008,** *3* (1), 55-68.

[30]   A. Talapatra, N. Singh, A. O. Adeyeye, *Phys. Rev. Appl.* **2020,** *13* (1).

[31]   D. M. Arroo, J. C. Gartside, W. R. Branford, *Phys. Rev. B* **2019,** *100* (21).

[32]   Y. Li, G. Gubbiotti, F. Casoli, S. A. Morley, F. J. T. Gonçalves, M. C. Rosamond, E. H. Linfield, C. H. Marrows, S. McVitie, R. L. Stamps, *J. Appl. Phys.* **2017,** *121* (10).

[33]   M. Donahue, D. G. Porter, *OOMMF User's Guide, Version 1.0, Intergency Report NISTIR 6376* (National Institute of Standard and Technology, Gaithersburg, MD) http://math.nist.gov/oommf.

[34]   F. Montoncello, L. Giovannini, W. Bang, J. B. Ketterson, M. B. Jungfleisch, A. Hoffmann, B. W. Farmer, L. E. De Long, *Phys. Rev. B* **2018,** *97* (1).

[35]   J. C. Gartside, D. M. Arroo, D. M. Burn, V. L. Bemmer, A. Moskalenko, L. F. Cohen, W. R. Branford, *Nat. Nanotechnol.* **2018,** *13* (1), 53-58.

[36]   M. Krawczyk, D. Grundler, *J. Phys. Condens. Matter.* **2014,** *26* (12), 123202.

[37]   L. Fallarino, A. Oelschlägel, J. A. Arregi, A. Bashkatov, F. Samad, B. Böhm, K. Chesnel, O. Hellwig, *Phys. Rev. B* **2019,** *99* (2).

[38]   K. Chesnel, A. S. Westover, C. Richards, B. Newbold, M. Healey, L. Hindman, B. Dodson, K. Cardon, D. Montealegre, J. Metzner, T. Schneider, B. Böhm, F. Samad, L. Fallarino, O. Hellwig, *Phys. Rev. B* **2018,** *98* (22).

[39]   L. Landau, E. Lifshits, *Physikalische Zeitschrift der Sowjetunion* **1935**, *8*, 153-169.

[40]   C. Kittel, *Phys. Rev.* **1948,** *73* (2), 155-161.

[41]   W. M. Li, Y. Yang, Y. J. Chen, T. L. Huang, J. Z. Shi, J. Ding, *J. Magn. Magn. Mater.* **2012**, *324*, 1575-1580.

[42]   D. Kumar, A. O. Adeyeye, *J. Phys. D: Appl. Phys.* **2017,** *50* (34).

[43]   A. O. Adeyeye, N. Singh, *J. Phys. D: Appl. Phys.* **2008,** *41* (15).

Figure 1. (a) and (d) represent the SEM images for type-I and type-II arrays of nanomagnets respectively with magnified views as insets describing the dimensions, thickness-dependent hysteresis loops for type-I arrays at applied field angles (b) 0°, (c) 90° and type-II arrays at applied field angles (e) 0°, (f) 90°. The inset at the left-bottom corner of Fig. 1 (a) describes the geometry of the applied magnetic field relative to the arrays of nanomagnets.
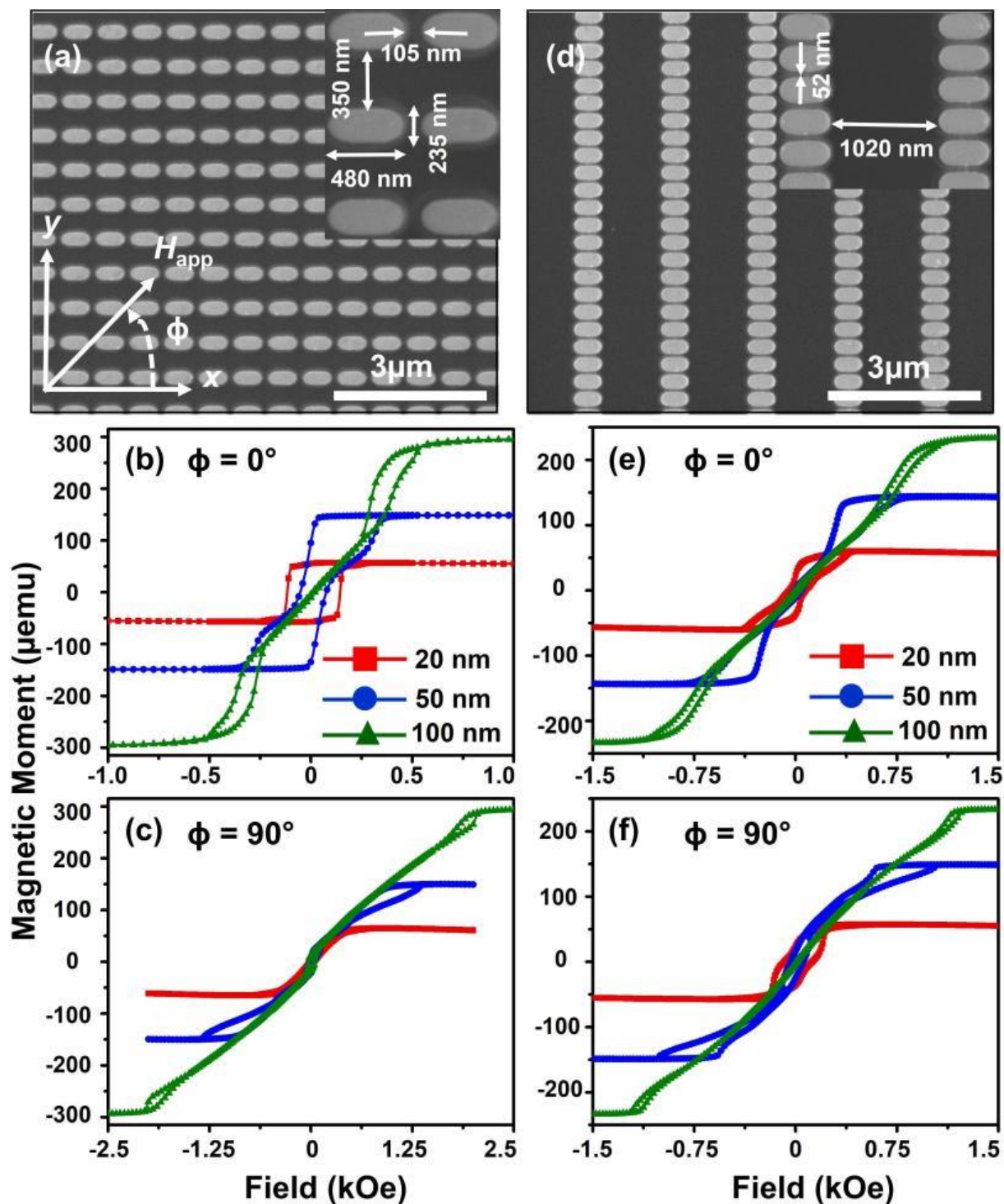
**Figure 2.** MFM images at remanence for two different applied field angles to establish the remanent state, (a) and (c) at 0°, (b) and (d) at 90° for type-I and type-II arrays respectively. The single vortex structures are designated with a dotted ellipse, elongated vortex by a dotted circle, and multiple vortices with a dotted rectangle. The scale-bar is identical for all the images.
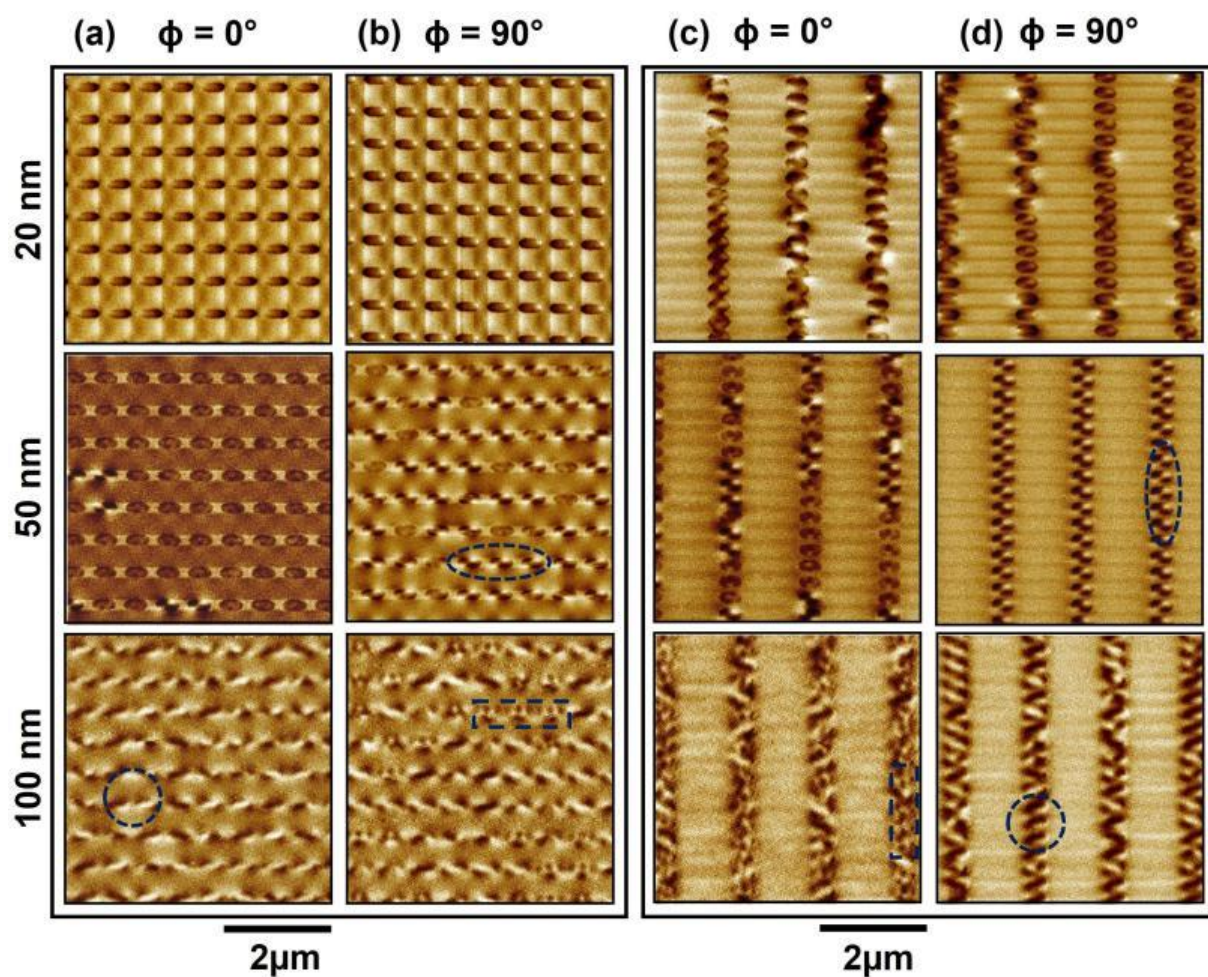
Figure 3. Thickness dependent simulated hysteresis loops for type-I arrays at applied field angles (a) 0°, (b) 90° and for type-II arrays at applied field angles (d) 0°, (e) 90°, (c) and (f) represent the snapshots of the spin-states at remanence for different thicknesses of the type-I and type-II nanostructures respectively for two different applied field angles.
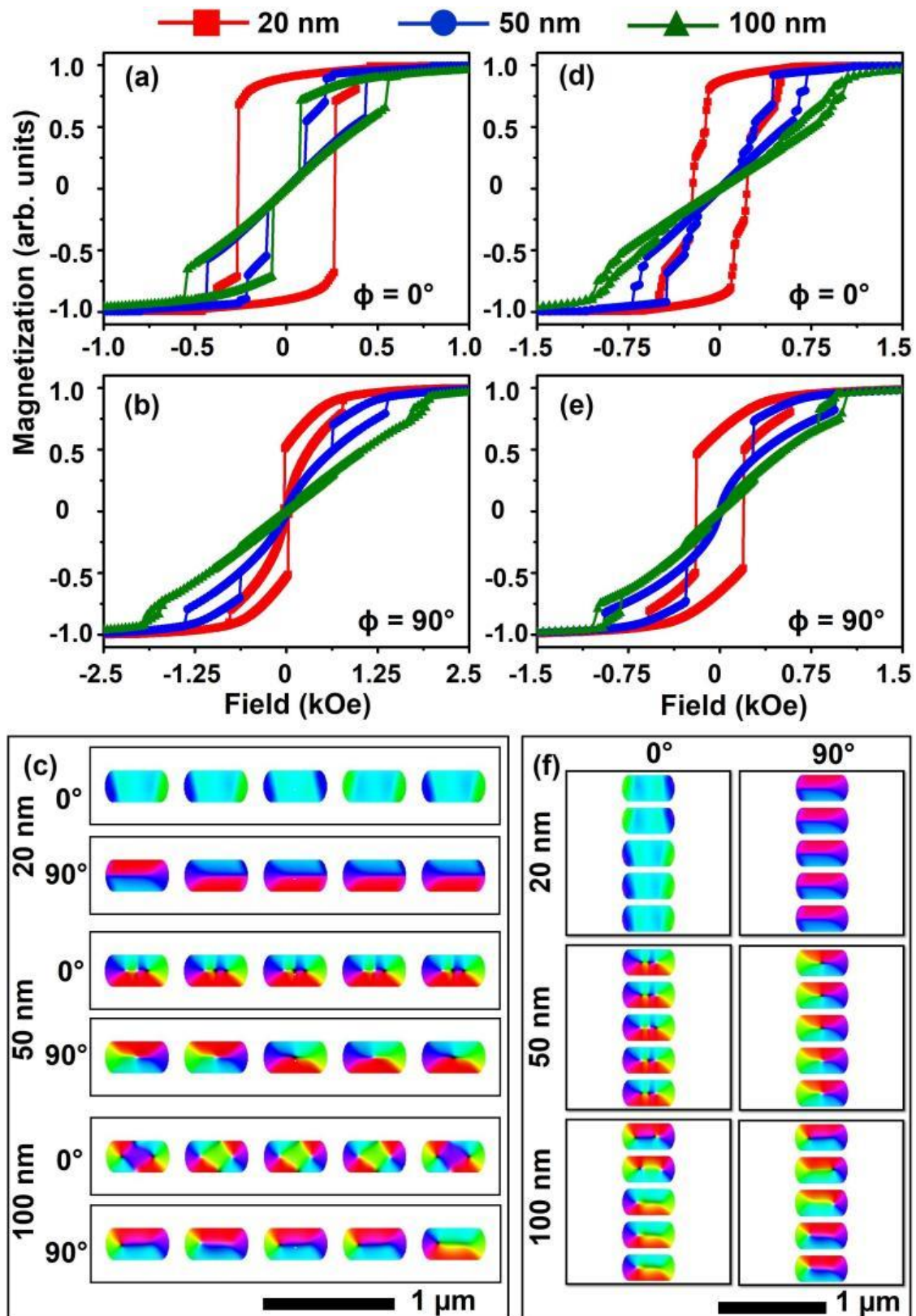
Figure 4. Representative ferromagnetic resonance spectra at 12 GHz for (a) type-I and (b) type-II arrays of ellipsoidal nanomagnets at different thicknesses and applied field angles. The corresponding structures are shown as insets. The first fundamental modes are designated with asterisks and the other low-intensity modes are designated with circles.
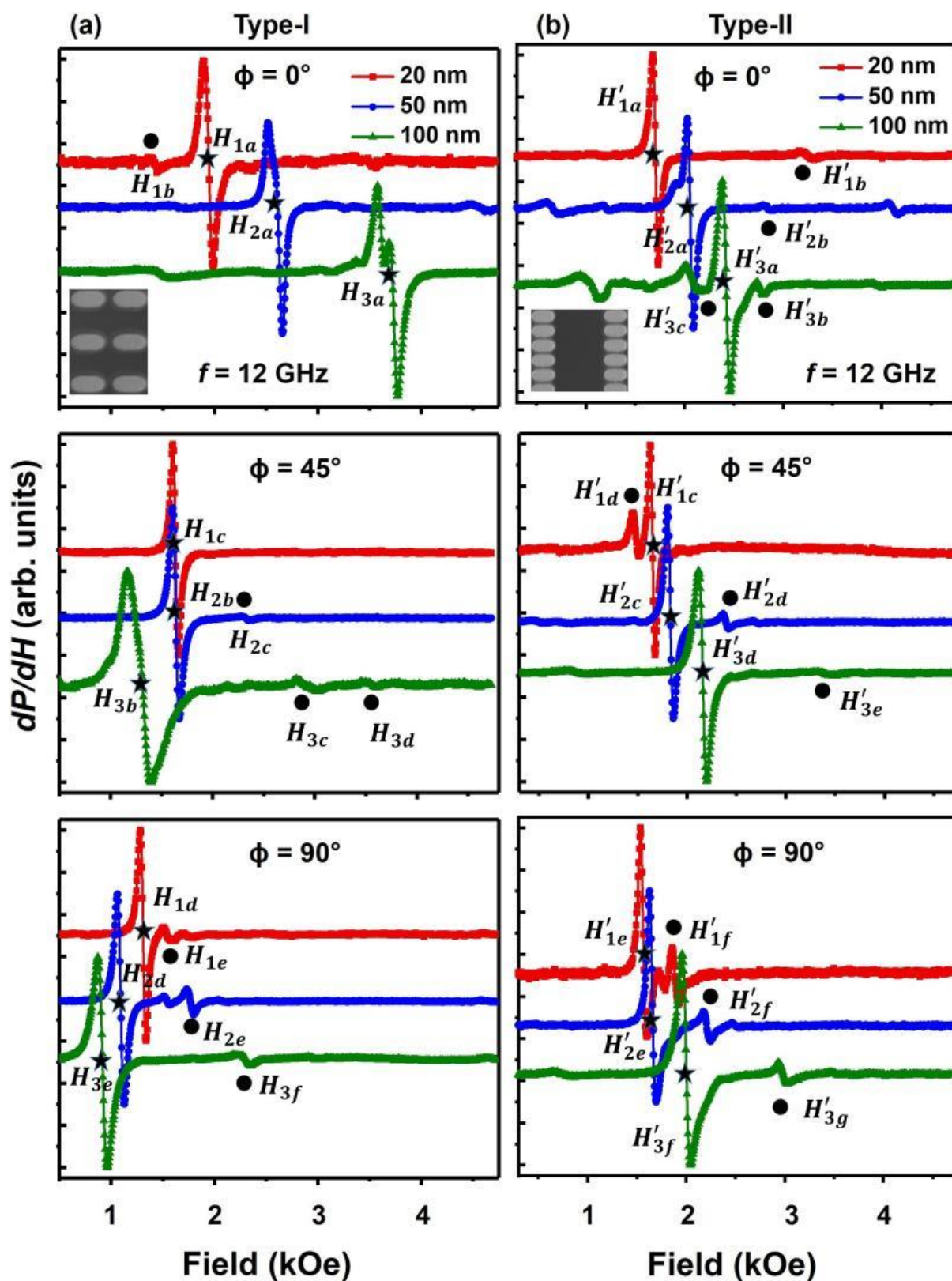
Figure 5. Variation of the resonance field with frequency for (a) type-I and (b) type-II arrays at different film thicknesses for applied field angles of 0°, 45°, and 90°. The corresponding structures are shown as insets.
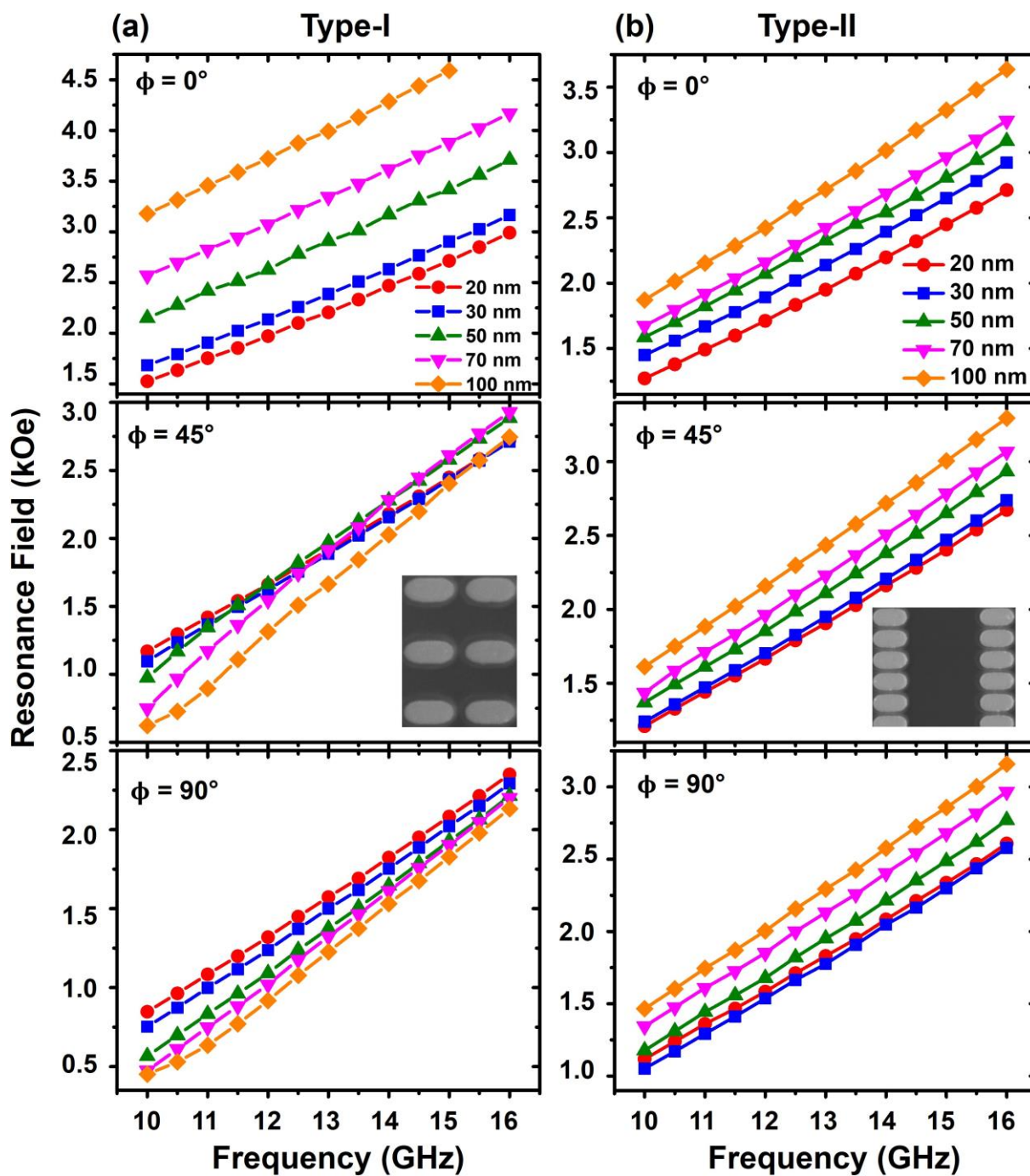
Figure 6. Simulated FMR response at 2.5 kOe for 50 nm thick (a) type-I and (c) type-II nanostructures at different applied field angles with the 2-D mode profiles at the designated resonance frequencies for (b) type-I and (d) type-II nanostructures.
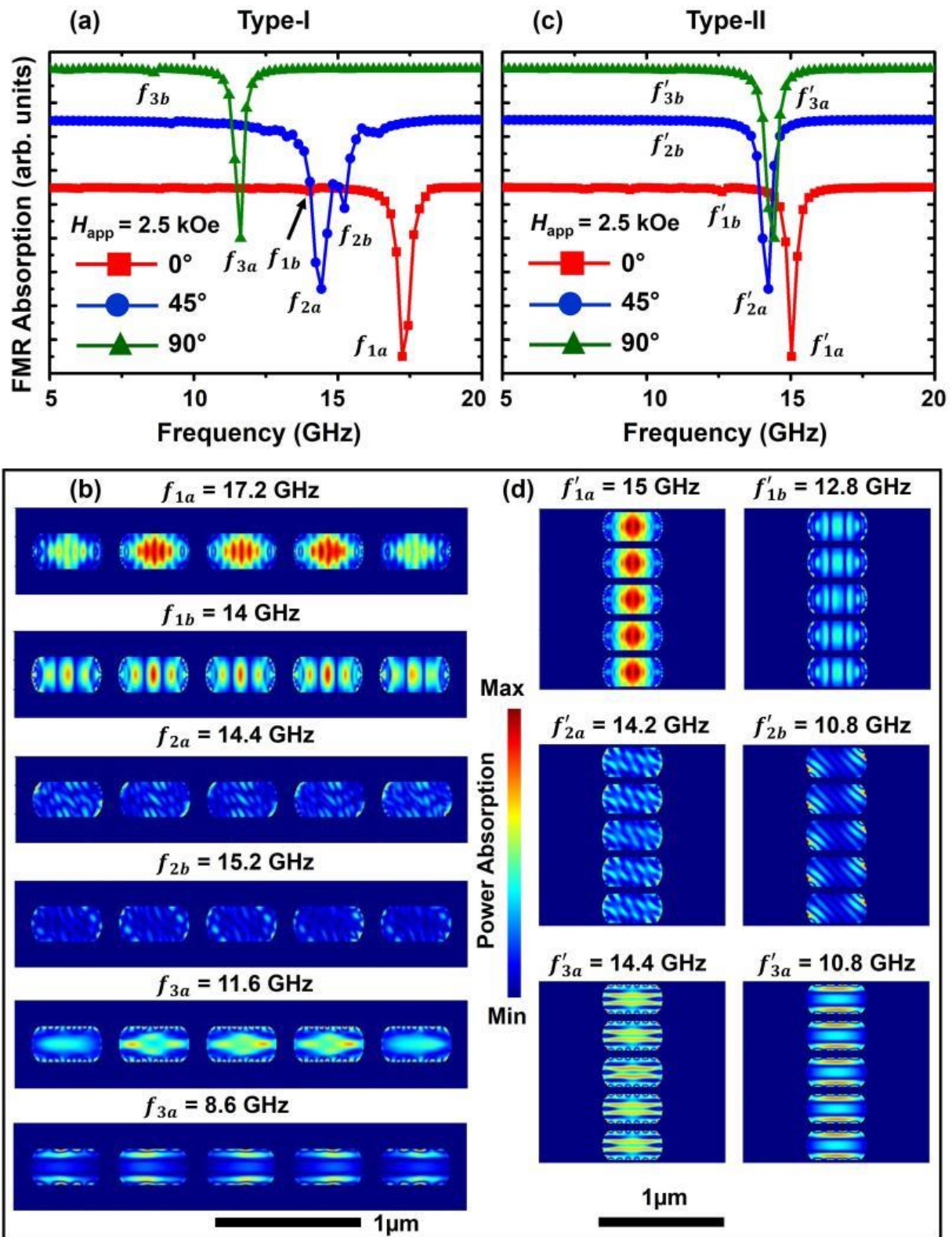
Table 1. Thickness-dependent variations of H_c, M_R/M_s, and H_s at different angles of applied in-plane magnetic field, obtained from the SQUID measurements.

d [nm]	ϕ [°]	H_c [Oe]		M_R/M_s [%]		H_s [Oe]	
		Type-I	Type-II	Type-I	Type-II	Type-I	Type-II
20	0	130	104	98.3	52	290	420
	90	20	62	7.4	50	1100	675
30	0	136	60	98	47.3	500	750
	90	15	21	4.3	11.8	950	900
50	0	64	24	77.1	4.6	600	925
	90	22	46	7.8	13.8	1400	1075
70	0	4	2	0	0	675	1075
	90	22	12	2.9	2.4	1650	1150
100	0	6	12	0	1.4	900	1150
	90	36	6	5.1	0	2150	1275

Table of Contents
Engineering the effective magnetic anisotropy of large area Permalloy linear chain arrays has been demonstrated with the variation in lattice arrangements and film thickness. Systematic investigations of static and dynamic magnetic properties established the complex interplay between the shape anisotropy and magnetostatic interactions. This work shows a potential application towards the reconfigurable magnonics and frequency tunable microwave devices.

Keyword Magnetic Materials, *x* Nanostructures

Abhishek Talapatra, Adekunle O. Adeyeye*

Linear Chains of Nanomagnets: Engineering the Effective Magnetic Anisotropy

ToC figure